# High-Temperature Corrosion of Stainless Steels and Ni Alloys During Combustion of Urea–Ammonium Nitrate (UAN) Fuel

M. Starostin[1] · A. Grinberg Dana[2] ·
O. Dinner[1] · G. E. Shter[1] · G. S. Grader[1]

**Abstract** This paper reports on corrosion behavior of different materials under combustion of a nitrogen-based fuel: aqueous solution of ammonium nitrate and urea (UAN). Tested materials include stainless steels 316, 310 and nickel alloys: 600, 601, 617, 800H and RA333. The results were derived under conditions close to those in practical continuous combustion applications. The coupons were positioned in quartz cylinders at temperature $520 \pm 10$ °C and pressure 10 MPa in the effluent gases. The corrosion of the 316 SS fuel injection tube was tested as a function of the stages that occurred along the tube, namely: heating, ignition, and combustion. Microstructure, chemical composition, depth profile and thickness of the formed oxide scales were studied. High corrosion resistance was found for 310 SS, nickel alloys 601 and RA 333. The heaviest corrosion attack of 316 inlet tube (both general and intergranular) was observed in the area where the exothermic combustion process began.

**Keywords** Nitrogen-based fuel · Corrosion · Stainless steel · Ni alloys

## Introduction

A low-carbon nitrogen-based alternative fuel in the form of an aqueous urea and ammonium nitrate (UAN) solution was previously reported as an alternative fuel that is nonexplosive, nontoxic, safe to handle, and can theoretically produce an

✉ G. S. Grader
grader@technion.ac.il

1    The Wolfson Department of Chemical Engineering, Technion—Israel Institute of Technology, 3200003 Haifa, Israel

2    The Nancy and Stephen Grand Technion Energy Program, Technion—Israel Institute of Technology, 3200003 Haifa, Israel

environmentally friendly effluent gas consisting of 73.0 % $H_2O$, 21.6 % $N_2$, and 5.4 % $CO_2$ (mole basis) upon combustion [1–6]. The aqueous UAN solution is a common fertilizer, and corrosion investigations of different materials in this solution at a relatively low temperature of 20–80 °C were previously published [7–10]. Stainless steels (SS) such as 304 and 316 showed the highest corrosion resistance at these temperatures [10]. However, high temperatures (up to 800 °C) and high pressures, as well as high water content may lead to poor SS corrosion resistance. Moreover, during combustion the chemical environment contains various gases such as $H_2O$, CO, $CO_2$, $N_2$, $NO_x$, $O_2$ as well as other short-lived radical species [1, 11, 12]; therefore, results of corrosion studies conducted at high temperatures in air [13, 14] and other oxidation environments [15–18] are insufficient for metal characterization at UAN combustion. The literature on corrosion resistance of materials in such environment is practically absent; therefore, it is driving a re-examination of traditional alloys.

The first corrosion resistance study during continuous aqueous UAN combustion at 550–750 °C and 20 MPa for several SS (316, 310 and 330) was presented previously [19]. In that study, experiments were done under cyclic conditions for 200 h, 25 cycles of 8 h each. A highly turbulent gas flow regime was observed in the low reactor zone at high ($\sim$750 °C) temperature near the combustion products outlet from the fuel tube, while the gas flow regime was laminar in the upper reactor zone which was kept at 550 °C. The selected chromia-forming stainless steels (SS) failed to form a protective oxide layer in the tested conditions. No protective Cr-rich oxide films were found in the scales formed on any of the tested SS specimen. The double-layered scales formed on the SS specimens were porous, cracked, and non-uniform. Spalling of the oxide film was observed in all the examined SS samples. Corrosion attack was specifically heavy on the samples placed in the high-temperature turbulent reactor zone.

Nickel-containing materials tested in this work were selected for their higher corrosion and heat resistance in comparison with stainless steels. Nickel and nickel-based alloys are widely used in aircraft and power-generation turbines, rocket engines and other challenging environments, including nuclear power and chemical processing plants [20]. Wide usage of nickel-based alloys in modern industries is attributed to their ability to withstand a variety of severe operating conditions involving corrosive environments, high temperatures, high stresses, and combinations of these factors.

Nickel can accommodate larger amounts of alloying elements (mainly Cr, Mo, W) in solid solution as compared to iron. Therefore, nickel-based alloys in general can be used in more aggressive environments than SS. Chromium additions impart an improved resistance to oxidizing media and to high-temperature oxidation. Alloys with chromium concentration of more than 20 wt% showed better oxidation resistance due to the development of Cr-rich oxide layers [21]. Cobalt imparts unique strengthening characteristics to alloys designed for high-temperature service. Molybdenum also significantly improves the pitting and crevice corrosion resistance of nickel-based alloys. Silicon is typically present only in minor amounts in most nickel-based alloys as an element that improves high-temperature oxidation resistance. Aluminum and titanium are often used in minor amounts in corrosion-

resistant alloys for increasing oxidation and nitriding resistance as well as carbon binding. Iron is typically used in nickel-based alloys to reduce costs, not to promote corrosion resistance. Although nickel alloys are more expensive than iron-based alloys, their excellent performance characteristics of heat and corrosion resistance often makes them the most economical, long-term choice.

Iron–nickel-based alloy 800 (Incoloy) is one of the most widely used alloys in the energy and petrochemical industries. It is also used in a variety of applications involving exposure to corrosive environments and high temperatures. It is resistant to oxidation, carburization and other types of high-temperature corrosion, and it is a widely used material for construction of equipment requiring corrosion resistance, heat resistance, strength, and stability for service up to 816 °C. This material, hence, was recently recommended as a candidate material for the generation IV nuclear power plants [22–24], bringing about more challenging conditions for its high-temperature applications. Alloy 800H is one of the preferred steam generator tube materials for Canada Deuterium Uranium reactors and the reactors in Germany and China. It is used extensively in other pressurized water reactor due to its superior kinetic stabilities under nuclear steam generator conditions. Results show that Alloy 800H is more resistant to surface oxidation than 316 SS in continuous supercritical water flow conditions at 650 °C and 25 MPa, forming a thinner and more stable oxide scale.

The most common corrosion-resistant Ni–Cr materials, with higher Ni content than Incoloy 800, are Inconel alloys series 600 [25]. They are typically used for furnace components, chemical and food processing, aerospace and land-based gas turbine parts like jet engines, and other extreme-service applications.

Inconel alloy 600 ($\sim$73 wt% Ni, $\sim$16 wt% Cr) is a stable, austenitic solid–solution alloy with good oxidation resistance at elevated temperatures. It is used for Pressurized Water Reactor (PWR) and steam generator tubing for the majority of PWR nuclear power stations. Alloy 600 is also used in Boiling Water Reactor (BWR) systems for different components and it is widely used for ammonia atmosphere [26].

In spite of their excellent general corrosion resistance, the above-mentioned alloys have been found to be susceptible to localized forms of corrosion attack such as stress corrosion cracking, corrosion fatigue, and intergranular attack. The corrosion behavior is similar to that of other austenitic alloys since the material can be prone to intergranular attack in some aggressive media by exposure to temperatures of 510–760 °C [27].

Inconel alloy 601 ($\sim$62 wt% Ni, $\sim$23 wt% Cr) in conjunction with $\sim$1–1.5 wt% content of aluminum gives the alloy superior resistance to high-temperature corrosion. Of particular significance is its resistance to oxidation at temperatures up to 1200 °C [28]. By virtue of its contents of chromium and aluminum, alloy 601 offers unique resistance to oxide spalling under cyclic thermal oxidation. The superior oxidation resistance of Inconel alloy 601 is related to the amounts of nickel, chromium, and aluminum in the alloy [29–31]. During high-temperature exposure, these elements form an extremely protective and adherent oxide film on the surface of the material. Alloy 601 is widely used in contaminated combustion environments.

Inconel alloy 617 has the lowest Fe content ($\sim 1$ wt%) in comparison to the 800, 600 and 601 alloys [32]. The high Ni ($\sim 55$ wt%) and Cr ($\sim 22$ wt%) contents together with Mo ($\sim 9$ wt%), Co ($\sim 12$ wt%), and $\sim 1$ wt% Al provide the alloy with a high resistance to a variety of reducing and oxidizing environments at elevated temperatures. The 617 nickel alloy has been developed for very high-temperature applications in excess of 800 °C. Several studies of Alloy 617 behavior in different corrosive environments at high temperature were published [33–36]. The alloy was used in nitric acid and petrochemicals production and it became one of the candidate materials for structural components in high-temperature gas-cooled reactor designs.

A high-chromium–nickel-based alloy RA 333 ($\sim 45$ wt% Ni, $\sim 25$ wt% Cr, $\sim 3$ wt% Mo, $\sim 3$ wt% Co and $\sim 3$ wt% W) has excellent oxidation and hot corrosion resistance [37, 38]. RA333 is a fully austenitic material and cannot be hardened or strengthened by heat treatment. RA333 has been the choice for all types of applications that require heavily carburizing atmospheres. Fabrications including radiant tubes, corrugated boxes and furnace belt pins have all been made from RA333 to withstand the high-carbon potentials within these atmospheres. RA333 has tolerable resistance to boiling nitric acid.

The present work is a significant step forward in the systematic corrosion performance investigation [19] of different alloys under continuous UAN fuel combustion. The behavior of austenitic SS 316L (USN S31600), 310S SS (UNS S31008) and five nickel alloys: 600 (UNS N06600), 601 (UNS N06601), 617 (UNS N06617), 800H (UNS N08810) and RA333 (UNS N06333) is reported at 520 °C and 10 MPa. To the best of our knowledge, the effect of intermediate products formed during UAN fuel ignition and combustion on corrosion was not studied. In the present work, this effect was evaluated using a fuel inlet tube made of 316 SS, in which the fuel ignited, by investigation of the oxidation behavior of different segments along the tube. The 316 SS material was selected to serve as the inlet tube, since it is more sensitive to changes of the temperature and media composition.

## Experimental Procedures

Corrosion coupons of AISI 316L, 310S, and Ni alloys 600, 601, 617, 800H, RA 333 with 600 grit surface finish were supplied by Metal Samples Company (USA). The chemical compositions provided by the suppliers are listed in Table 1. Rectangular flat samples were $20 \times 15$ mm with a thickness of 3 mm. The specimens were cleaned with acetone, washed with deionized water, and dried in air prior to the experimental series.

A highly concentrated aqueous UAN solution composed of 60 wt% ammonium nitrate (AN), 15 wt% urea and 25 wt% water was prepared using analytical grade AN (Sigma Aldrich), urea (Sigma Aldrich) and distilled water. The pH of the initial solutions was 5.8–6.0.

Corrosion resistance of the tested materials was investigated under continuous combustion conditions for 100 h. The continuous reaction system consisted of a fuel tank equipped with a high-pressure pump (SSI, USA), a high-pressure and high-

**Table 1** Chemical composition of the investigated alloys (wt%)

| Alloy | C | Fe | Cr | Ni | Mo | Mn | Si | Co | Cu | Al | Cb | Ti | W |
|-------|-----|-------|-------|-------|-------|------|------|-------|------|------|------|------|------|
| AISI 316L | 0.018 | 68.83 | 16.90 | 10.01 | 2.04 | 1.52 | 0.24 | – | 0.43 | – | – | – | – |
| AISI 310S | 0.062 | 54.15 | 24.17 | 19.45 | 0.080 | 1.36 | 0.64 | – | 0.07 | – | – | – | – |
| Incoloy 800H | 0.07 | 46.70 | 20.56 | 30.60 | – | 0.54 | 0.32 | – | 0.03 | 0.52 | – | 0.57 | – |
| RA 333 | 0.055 | 18.5 | 24.53 | 44.82 | 3.05 | 1.53 | 1.25 | 2.85 | 0.03 | 0.16 | 0.02 | – | 3.06 |
| Inconel 617 | 0.06 | 1.03 | 21.93 | 54.66 | 8.84 | 0.18 | 0.12 | 11.71 | 0.02 | 0.96 | – | 0.49 | – |
| Inconel 600 | 0.052 | 9.04 | 16.11 | 72.95 | – | 0.22 | 0.5 | 0.52 | 0.01 | 0.05 | 0.13 | 0.21 | – |
| Inconel 601 | 0.1 | 12.14 | 23.01 | 61.12 | – | 0.81 | 0.54 | – | 0.51 | 1.4 | – | 0.37 | – |

temperature vertical 500-ml reactor vessel (Parr, USA), a gas receiver (11.5 L), a programmable logic controller (PLC) and an FTIR system (Gasmet, Finland) for the gaseous products online analysis. The reactor was externally heated in a vertical furnace to 450 °C, and the temperature inside the reactor was measured using a thermocouple located near the specimens. A general view of the reactor is shown in Fig. 1a, c. The 170-mm-long fuel inlet tube made of 316 SS, in which the monofuel ignites, was placed vertically top-down inside the reactor [4]. The fuel was fed at a constant rate of 4 ml/min. Comprehensive details concerning this reaction system and gas analysis can be found elsewhere [1].

The specimens were placed in the central reactor part in quartz cylinders located on a ceramic plate (Fig. 1a, b). This setting allowed excluding the turbulent gas flow near the samples and keeping them at a constant flow and a temperature of 520 ± 10 °C, as well as preventing the transfer of corrosion products between specimens. The temperature inside the reactor was measured by a thermocouple positioned near the specimens.

As previously shown [1, 4], the ignition and combustion processes of a monofuel such as aqueous UAN occur inside the fuel inlet tube which was screwed into the reactor cover (Fig. 1a, c). As the fuel enters the preheated inlet tube it ignites and the temperature increases [3] inside the tube. The initial elementary reactions during the combustion of aqueous UAN form corrosive intermediate products [1], as described by the following reactions:

$$NH_4NO_3 \Leftrightarrow NH_3 + HNO_3 \tag{1}$$

$$HNO_3 \Leftrightarrow OH + NO_2 \tag{2}$$
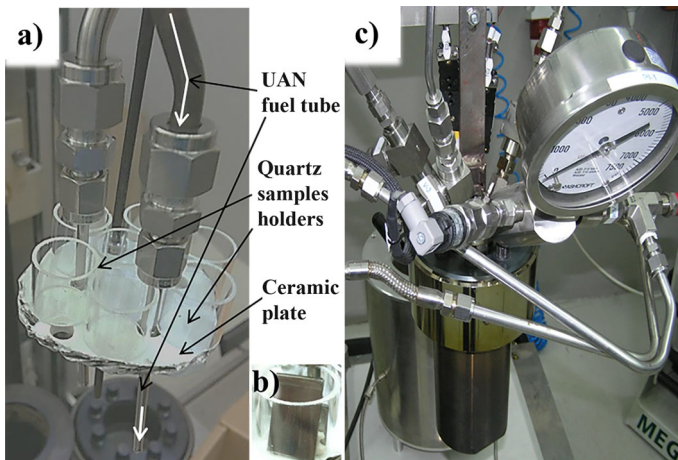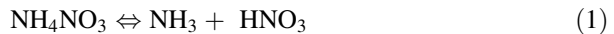


**Fig. 1** A view **a** of the setting inside the reactor, depicting the samples' quartz cylinders and the fuel inlet tube, the *white arrow* indicates the fuel flow direction in inlet tube; **b** a specimen in the quartz cylinder before test and **c** a general view of the closed reactor

$$NH_2CONH_2 \Leftrightarrow HNCO + NH_3 \qquad (3)$$

The principal reactions of aqueous UAN combustion including all possible intermediate products are described elsewhere [1–3, 5, 6, 11, 12]. The final product composition by volume at the reactor outlet under the conditions reported above, as detected by the FTIR gas analyzer, was the following (theoretical values for complete reaction appear in parenthesis): 68 % water (73.0 %), 5.4 % $CO_2$ (5.4 %), 0.5 % $N_2O$, 285 ppm CO, 914 ppm NO, 114 ppm $NH_3$, while the remaining $\sim 25$ % is attributed to $N_2$, $O_2$, and $H_2$ (21.6 % for $N_2$). While this fuel could emit a more environmentally friendly effluent even without a post-catalytic treatment [1, 4], the working conditions of 4 ml/min and 10 MPa with the above product composition were chosen to establish conservative results at a relatively high-corrosion environment.

Before and after the experiment, the reactor was purged with nitrogen, and condensation prior to cooling was avoided. After the full experiment duration, the specimens were cleaned with acetone, washed with deionized water and dried in air to assure that the investigated surfaces are cleaned from deposited particles (i.e., from the ceramic plate, Fig. 1a), and that they are ready for the metallographic investigation. This light cleaning procedure did not affect the scale formed on the metal surface. The sample mass change was determined by weighing before and after the exposure and was performed with VIBRA HT analytical balance with precision of 0.1 mg.

A corrosion effect of the reaction intermediates was studied by an investigation of several sections of the fuel inlet tube in which the ignition and combustion processes occurred. After the experiment, the fuel inlet tube was cut into seven parts (Fig. 2). The top fuel tube section from the UAN entrance up to the connector before point 5 was 6.4 mm in diameter with a thickness of 1.6 mm. The diameter of the lower section of the fuel tube following the connector was 3.14 mm with thickness of 0.6 mm. Cross sections made according to Fig. 2 were used for the metallographic investigation.

Studying the metallographic samples (coupons and tube cross sections) included their inspection with HRSEM (ZEISS Ultra Plus FESEM, GEMINI), equipped with EDS (Bruker-AXS Microanalysis GmbH). The cross sections were polished up to 1 μm surface finish. Etching was performed by Marble's reagent—50 ml HCl, 10 g $CuSO_4$ in 50 ml $H_2O$ (SS)—allowing the investigation of the microstructure.



**Fig. 2** Side view of the 170-mm-long 316 SS inlet tube in which the aqueous UAN fuel ignition and combustion occurred

## Results

### Fuel Inlet Tube (316 SS)

The UAN fuel inlet tube was screwed into the inner surface of the reactor head. Therefore, at a flow rate of 4 ml/min [1] used herein, heating and ignition of the aqueous UAN fuel occurred immediately as the fuel entered the inlet tube.

Three representative parts of the fuel inlet tube are shown in Fig. 3 after the test: (a) UAN entrance (Fig. 2); (b) fracture of the tube part screwed into the reactor cover (2, Fig. 2); (c) outlet of gases after the UAN combustion (Fig. 2).

The SEM images of the cross sections prepared from the fuel tube (Fig. 2) are shown in Figs. 4, 5, 6, 7, 8, 9. These figures reveal an inner scale in addition to an outer corrosion scale that formed on the 316 SS tube during aqueous UAN combustion. The exposure temperature and, mainly, the medium composition changed along the tube, and lead to different corrosion attacks and surface scales. It is important to note that due to the large differences in the corrosion type and scale thickness, the SEM micrographs were taken at different suitable magnifications. Figures 4, 5, 6, 7, 8, and 9 demonstrate how the corrosion scales and structure changes along the 316 SS fuel inlet tube during 100-h test.

SEM micrographs of cross section 1 (Fig. 2) are shown in Fig. 4.

A minor corrosion attack was found in this area, where the fuel's heating only initiates. However, only few millimeters away, (cross section 2, Fig. 2), very heavy corrosion was observed (Fig. 5). The SEM analysis revealed that the heaviest
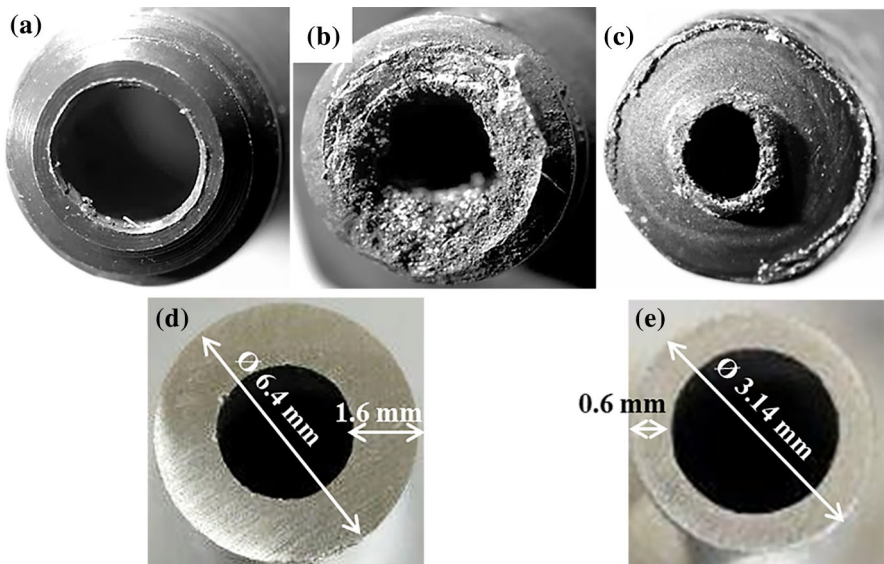


**Fig. 3** Front views of three representative fuel inlet tube sections: **a** UAN entrance (Fig. 2); **b** fracture of tube part screwed into the reactor cover (point 2, Fig. 2); **c** outlet of gases after the UAN combustion (point 7, Fig. 2); **d** cross section of the entrance fuel tube part; **e** cross section of the gas outlet fuel tube part (Fig. 2)
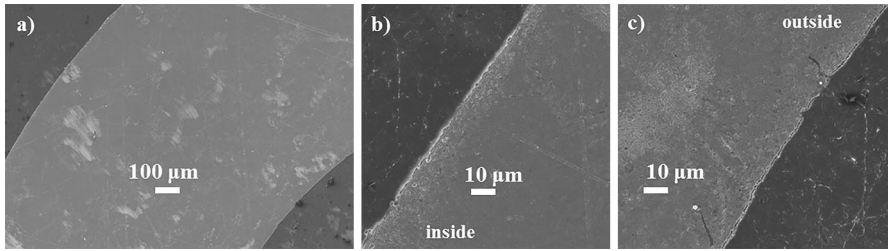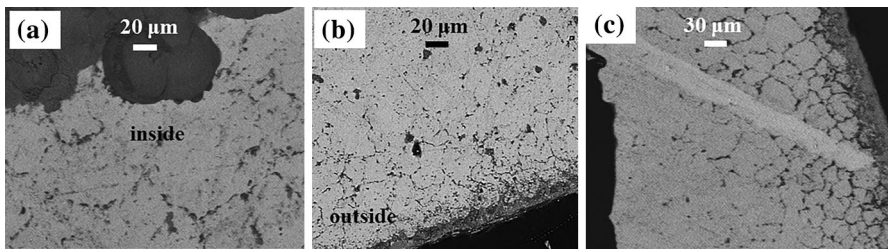
**Fig. 4** SEM images of cross section 1 (Fig. 2) at different magnifications
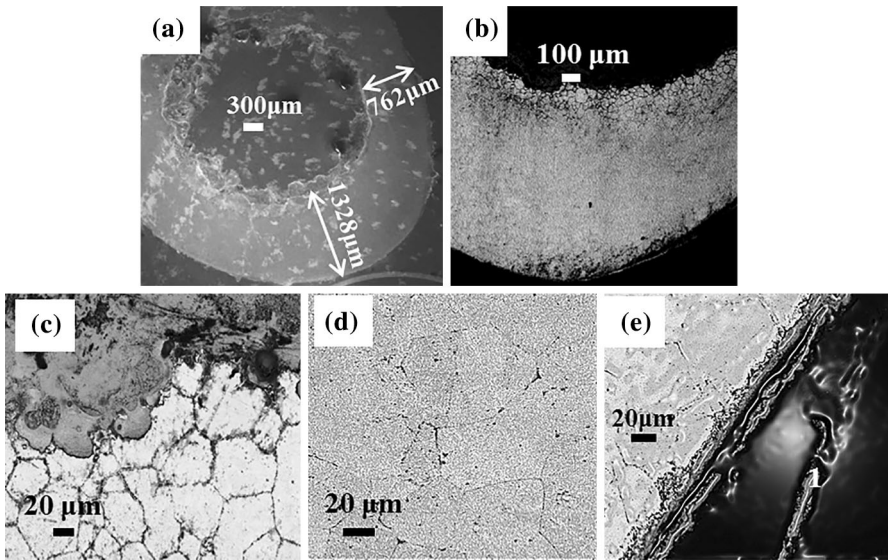


**Fig. 5** SEM images of cross section 2, part threaded in reactor cover (Fig. 2): **a, b** front view; **c** inside tube part; **d** central of tube wall; **e** outside tube wall



**Fig. 6** SEM images for cross sections 3 and 4 (Fig. 2): **a** the inner surface of cross section 3; **b** the outer surface of cross section 3, and **c** the outside surface of cross section 4

corrosion attack occurred in the area of cross section 2, where the hot fuel ignition commenced. This is explained by the presence of the different intermediates, including corrosive $NO_x$ that are formed in the first stages of aqueous UAN
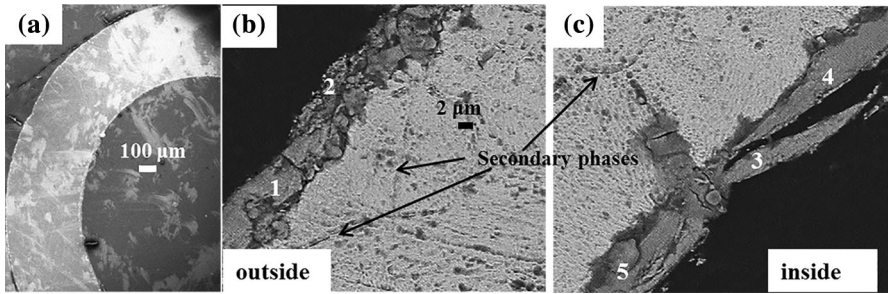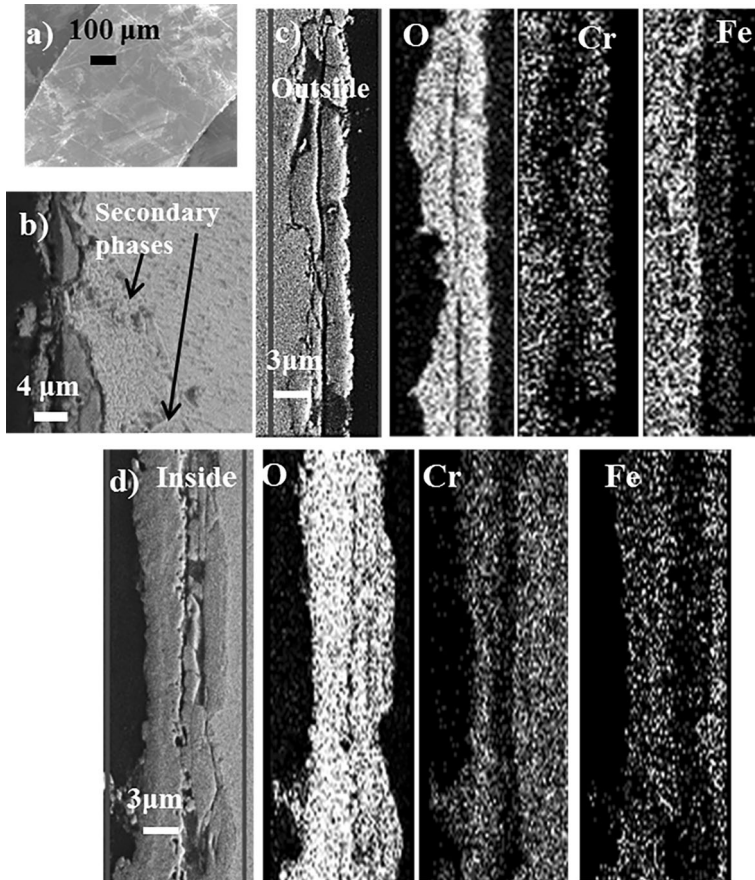
Fig. 7 SEM micrographs of cross section 5: **a** general view; **b** tube outside surface, and **c** tube inside surface
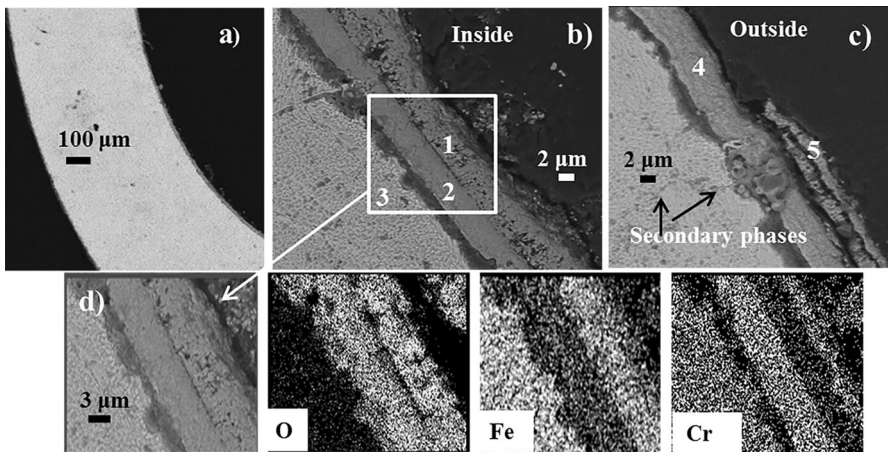


Fig. 8 SEM micrographs of cross section 6 (Fig. 2): **a** general view; **b** inside tube part; **c** outside tube part, **d** inside tube part marked in (**b**) and EDS mapping for O, Fe and Cr

combustion [1]. Figure 5 shows typical SEM micrographs of cross section 2 after 100-h test. In some zones, the tube wall thickness decreased by a factor of x2 (about 762 µm Fig. 5a, relative to 1.6 mm, Fig. 3d). A heavy internal attack (Fig. 5c–e) observed for the whole tube thickness up to the external part indicates noticeable temperature increase during ignition [2]. High temperatures in the range 510–780 °C provoke microstructural changes in SS, increasing the susceptibility to intergranular corrosion (IGC) [39]. This form of corrosion results in loss of strength in metal parts where the grains have fallen out. After the test, the fuel inlet tube was easily broken out by hand in the area of the cross section 2 (Fig. 3b).

The IGC can also be seen in the cross sections 3 and 4 (Fig. 6). Here, IGC was also observed for the entire cross section of the inlet tube. However, only an appearance of secondary phases in the boundary zones was found in the cross sections 5–7 (Figs. 7, 8, 9). It is noted that the temperature can decrease significantly in the segments 5–7 compared to the temperature of the segments 2–4, where the fuel ignites. The joint effect of high ignition temperature and

**Fig. 9** SEM micrographs of cross section 7 (Fig. 2): **a** general view; **b** outside tube part after etching; **c** outside; **d** inside tube part and EDS mapping for O, Fe and Cr

formation of corrosive intermediate products [1–3, 6, 11, 12] leads to the heavy IGC in this segment.

An EDS analysis of the inner and outer surfaces of the cross sections 5–7 showed that these surfaces were covered with Fe/Cr/Ni oxide films of different compositions (Figs. 7, 8, 9, Tables 2, 3). EDS mapping (Figs. 8d, 9d, e) and analysis in several points (Fig. 8b, Table 3) on the inner and outer surfaces of the cross sections 6 and

**Table 2** EDS analysis (wt%) in points as marked in Fig. 7a, b

| Point | O | Al | Si | Cr | Fe | Ni |
|---|---|---|---|---|---|---|
| 1 (Fig. 7a) | 29.84 | 0.21 | 0.87 | 29.16 | 32.06 | 7.86 |
| 2 (Fig. 7a) | 28.05 | 0.50 | 1.06 | 13.81 | 51.08 | 5.5 |
| 3 (Fig. 7b) | 32.05 | 0.15 | 0.90 | 25.70 | 38.19 | 3.01 |
| 4 (Fig. 7b) | 31.70 | 0.07 | 0.89 | 25.33 | 36.15 | 5.86 |
| 5 (Fig. 7b) | 32.55 | 0.06 | 0.75 | 16.02 | 43.69 | 6.93 |

| Table 3 Chemical composition (wt%) according to EDS results for points indicated in Fig. 8b, c | Area | O | Si | Mn | Cr | Fe | Ni | Mo |
|---|---|---|---|---|---|---|---|---|
| | 1 (Fig. 8b) | 34.26 | 1.28 | 0.21 | 1.89 | 61.63 | 0.47 | 0.26 |
| | 2 (Fig. 8b) | 31.97 | 0.85 | 0.75 | 28.84 | 28.01 | 8.40 | 1.18 |
| | 3 (Fig. 8b) | 1.69 | 0.92 | 2.14 | 18.08 | 62.67 | 12.32 | 2.18 |
| | 4 (Fig. 8c) | 30.12 | 1.03 | 1.12 | 27.16 | 33.43 | 5.43 | 1.71 |
| | 5 (Fig. 8c) | 37.03 | 0.85 | 0.31 | 2.34 | 59.47 | – | – |

7 (Figs. 8, 9) indicate that the alloy surface was covered by a Cr-rich oxide scale. However, in some areas the Cr-rich oxide film was covered by a Fe-rich oxide film. This fact reveals that Cr was depleted from the oxide scale, and the protective layer broke down.

Overall, the heaviest corrosion of 316 SS (both intergranular and general) was observed in the upstream parts of the fuel inlet tube, while in the downstream parts only general corrosion and the secondary phase appearance were found.

## The Tested Alloys

After 100 h of exposure to the combustion products inside the reactor, all specimens were covered with a black layer, which remained on the surface after cleaning with acetone and deionized water. A visual inspection did not reveal any obvious signs of oxide spallation on any of the investigated samples. The measured mass gain is shown in Fig. 10. The lowest oxidation rate ($<0.1$ mg/cm$^{-2}$) was found for the Ni/Cr-based alloy RA 333, followed by SS 310S and Ni alloy 601 (0.2 mg/cm$^2$). SS 316L exhibited the highest mass gain (0.42 mg/cm$^2$), while the two Ni alloys Ni 600 and Ni 800H showed the same results (0.4 mg/cm$^2$) and Ni 617 is about 0.37 mg/cm$^2$.

Evaluation of high-temperature corrosion is based not only on weight change but additionally on metallographic examination because of the presence of complex gaseous species. Moreover, the relatively high H$_2$O percentage in the combustion products as well as the relatively high temperature can also result in the establishment of grain boundary internal corrosion.
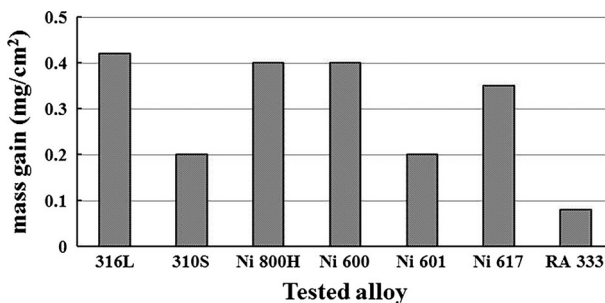


Fig. 10 Normalized mass gain of the tested alloys exposed for 100 h in the reactor
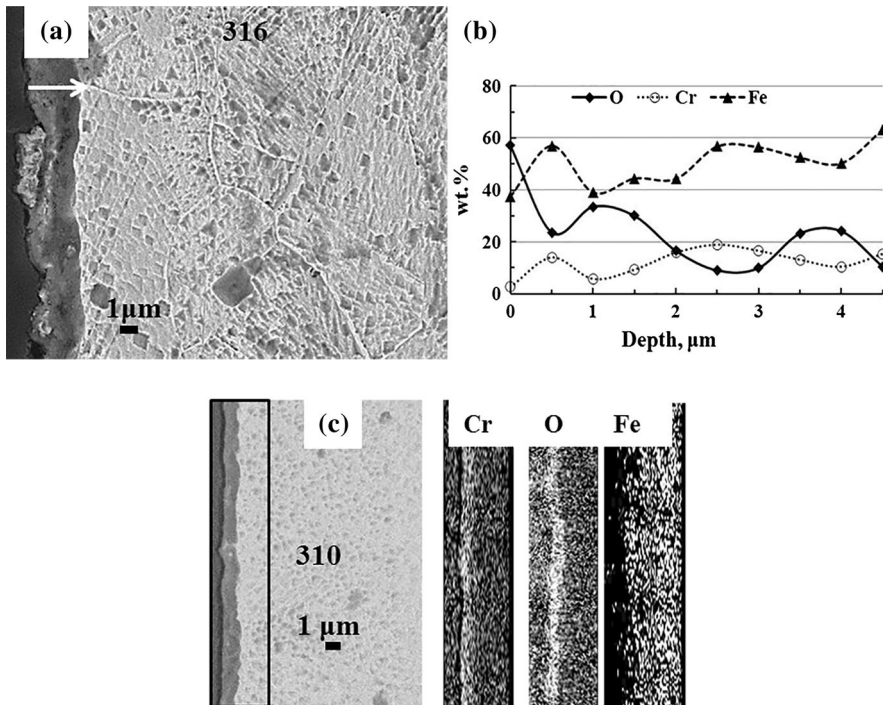
**Fig. 11** SEM micrographs of an oxide scale formed on 316 and 310 SS exposed to the reactor for 100 h: **a** oxide scale on 316 SS; **b** EDS analysis along the scan shown in (**a**); **c** oxide scale on 310 SS and corresponding elemental maps for oxygen, chromium and iron

Figure 11 compares the SEM cross-sectional images of the two stainless steels 316 and 310. A 2–3.5-μm-thick layer was formed on the 316 SS surface (Fig. 11a) after 100-h exposure in the gas mixture emerging from the UAN tube. A line scan EDS analysis for oxygen, iron and chromium (Fig. 11b) along the marked white arrow in Fig. 11a shows that a film consisting mainly of Fe-oxide was formed on the surface of the 316 SS samples. This film contains only minor amounts of Cr oxide, hence it is not protective. The weakly visible grain boundaries were observed for the 316 SS specimen, similar to those found in the cross sections 5–7 of the fuel inlet tube (Figs. 2, 7, 8, 9) made of 316 SS as well. On the other hand, according to the EDS mapping analysis the 310 SS exhibited on its surface a thin (<1 μm) protective Cr-rich oxide layer (Fig. 11c). Since 310 SS contains more than 20 wt% chromium, it had a better scaling resistance than conventional 316 SS.

The SEM image in Fig. 12 shows the microstructure and scale formed on Ni alloy 800H after 100-h exposure in the reactor. Localized oxidation was observed on the surface of alloy 800H. The EDS mapping of the scale for oxygen in Fig. 12b shows that the thickness of oxide film was 2–6 μm. According to EDS analysis (Fig. 12a and Table 4) the main constituent of the oxide film was Fe. In addition, a thick oxide scale can be subjected to spalling or cracking [21] and, therefore, cannot protect the alloy. The breakdown of the oxide film one can be seen in the top view
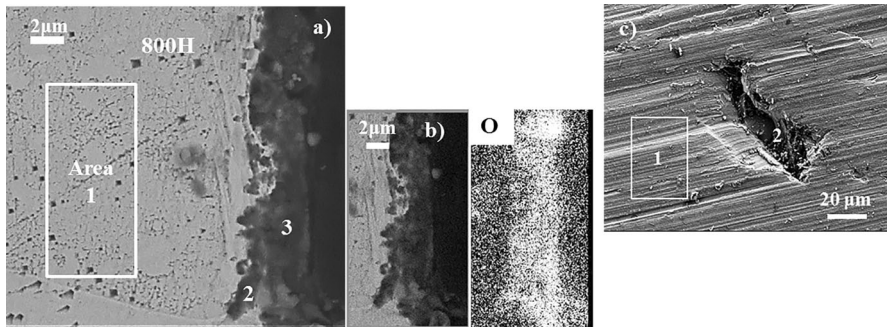
**Fig. 12** SEM micrographs of an oxide scale formed on Ni alloy 800H exposed to the reactor for 100 h: **a** oxide scale; **b** oxide scale and corresponding elemental maps for oxygen; **c** top view with breakdown of the scale
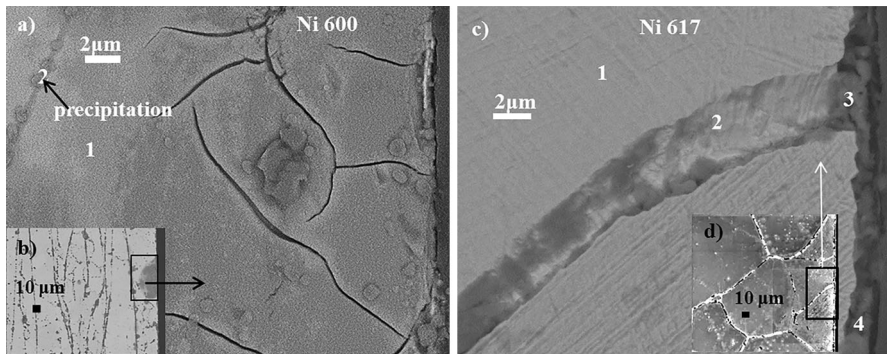
**Table 4** Chemical composition (wt%) by EDS for Ni alloy 800H matrix (Aria 1) and scale (points 2, 3 Fig. 12a and points 1, 2 Fig. 12c)

| Tested area | O | Al | Si | Ti | Mn | Fe | Cr | Ni |
|---|---|---|---|---|---|---|---|---|
| Area 1 (Fig. 12a) | 3.59 | 0.47 | 0.71 | 0.69 | 0.51 | 45.58 | 20.21 | 28.24 |
| 2 (Fig. 12a) | 34.02 | 0.28 | 0.76 | 0.20 | 0.35 | 38.41 | 13.25 | 12.73 |
| 3 (Fig. 12a) | 37.18 | 0.38 | 0.55 | 0.36 | 0.38 | 35.44 | 13.28 | 12.44 |
| Area 1 (Fig. 12c) | 17.56 | 0.96 | 1.35 | 0.89 | 1.55 | 36.41 | 23.20 | 18.07 |
| 2 (Fig. 12c) | 1.55 | 0.63 | 0.15 | – | 6.18 | 42.93 | 32.25 | 16.32 |

of the alloy 800 H (Fig. 12c, point 2). High Mn and low oxygen contents (Table 4) were found at this point. Healing of the oxide film was not observed and, therefore, localized corrosion occurred in the alloy 800. As a result, the oxide film formed on alloy Ni 800H cannot serve as a corrosion-protection layer under the tested conditions.

SEM micrographs of the cross section of alloys Ni 600 and 617 are presented in Fig. 13, and EDS analyses of the chemical composition in selected points on alloys 600 and 617 are listed in Table 5. No significant scale was visible on the surface of alloy 600.

However, the oxide layer thickness on the surface of alloy 617 was <1 µm (Fig. 13c), and it was >2 µm in surface area that was above the metallic grain boundaries. Intergranular corrosion was observed in the above-mentioned alloys at the tested conditions. Micrographs of cross section of nickel alloys 600 and 617 presented in Fig. 13 show deep internal oxidation along grain boundaries. Grain boundary segregation can be seen in Fig. 13a, b for Ni 600. In Inconel alloy 600, the grain boundaries have wavy appearance possibly due to the grain boundary formation of small amount of carbides, especially the Cr-rich phase (point 2, Fig. 13a). Susceptibility of alloy 600 to intergranular corrosion and intergranular corrosion stress corrosion cracking (IGSCC) has been described in the literature for both pressurized and boiling water reactors [24–27].

Fig. 13 SEM micrographs of an oxide scale formed on Ni alloys 600 and 617 after 100 h in the reactor: **a, b** alloy 600 at different magnifications, and **c, d** alloy 617 at different magnifications

Table 5 Chemical composition (wt%) by EDS for Ni 600 matrix (Fig. 13a, points 1, 2) and Ni 617 matrix (Fig. 13c, points 1, 2) and oxide scale (Fig. 13c, points 3, 4)

| Tested area | O | Al | Si | Cr | Mn | Fe | Co | Ni | Mo |
|---|---|---|---|---|---|---|---|---|---|
| 1 (Fig. 13a) | 5.45 | – | 0.5 | 16.59 | 0.41 | 10.08 | 0.52 | 66.45 | – |
| 2 (Fig. 13a) | 1.13 | – | 0.61 | 60.86 | – | 10.63 | | 26.77 | – |
| 1 (Fig. 13c) | 1.16 | 0.97 | 0.31 | 21.98 | – | – | 12.54 | 54.00 | 9.01 |
| 2 (Fig. 13c) | 1.48 | 0.58 | 0.50 | 19.51 | – | – | 11.59 | 56.20 | 10.05 |
| 3 (Fig. 13c) | 54.98 | 1.76 | 0.22 | 9.98 | – | – | 3.34 | 20.98 | 8.74 |
| 4 (Fig. 13c) | 55.27 | 0.97 | 0.38 | 10.70 | – | – | 3.76 | 21.58 | 7.34 |

As indicated in Fig. 13c, d, the microstructure of alloy 617 also contains continuous precipitates along the grain boundaries. Although alloy 617 contains >20 wt% Cr and additional elements such as Mo and Co, it did not demonstrate high corrosion resistance in the tested conditions. The high-temperature exposure of alloy 617 has been reported in previous works as a factor of enhancement in discontinuous precipitation of carbides, nitrides and carbo-nitrides on grain boundaries [33–36].

Nickel alloy RA 333 showed high corrosion resistance under the tested conditions, as a very thin protective layer (<1 μm) was formed on the alloy surface. The micrograph of the cross section is shown in Fig. 14a, a corresponding EDS map analysis for oxygen, tungsten and silicon in Fig. 14b, and a top view in Fig. 14c.

A very thin protective oxide film was also formed on the surface of alloy 601. The cross section and top view are shown in Fig. 15, and the chemical composition is given in Table 6.

EDS measurements were carried out at primary beam energies of 10 keV corresponding to probing depths of approximately 1 μm [40]. In the cases of RA 333 and Ni 601 (Figs. 14, 15), a scale thickness is below 1 μm was found. Therefore, the scale composition by EDS can be distorted by the matrix below the oxides layer. This fact should be taken on account when discussing the protection properties of the oxide layer formed on alloys RA 333 and Ni 601.
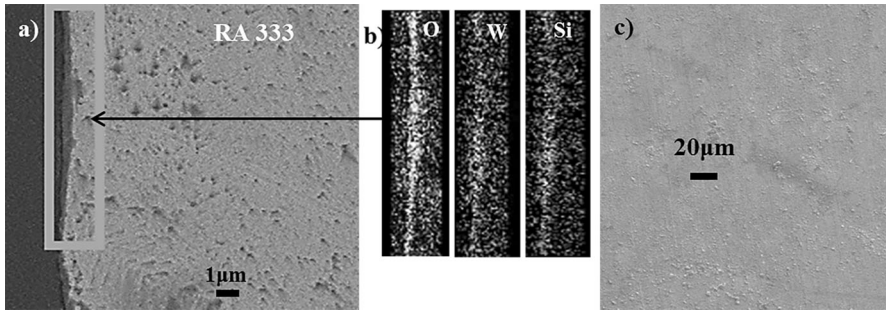
**Fig. 14** SEM micrographs of an oxide scale formed on Ni alloys RA 333 exposed to the reactor for 100 h: **a** oxide scale and **b** corresponding elemental maps for oxygen, silicon and tungsten; **c** top view after exposure
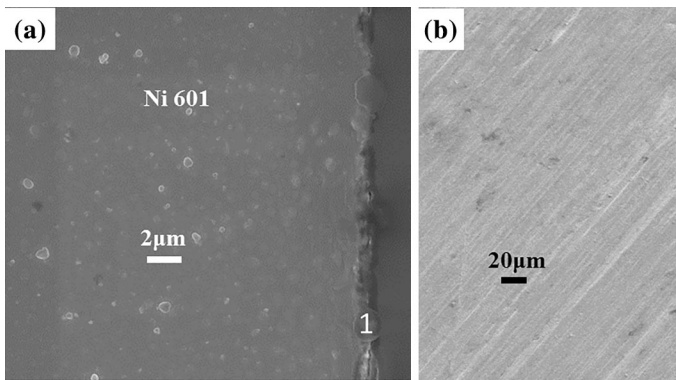


**Fig. 15** SEM micrographs of an oxide scale formed on Ni alloys 601 exposed to the reactor for 100 h: **a** oxide scale and **b** top view after exposure

**Table 6** Chemical composition by EDS (wt%): for top view of alloys RA 333 (Fig. 14c) and Ni 601 (Fig. 15b) before and after tests; for Ni 601 scale (Point 1, Fig. 15a) after test

| Tested area | O | Al | Si | Ti | Cr | Mn | Fe | Co | Ni | Mo | W |
|---|---|---|---|---|---|---|---|---|---|---|---|
| RA 333 (Fig. 14c) | 22.47 | – | 2.14 | – | 26.16 | 1.58 | 13.51 | 1.51 | 27.04 | 2.08 | 3.51 |
| RA 333 before test | 1.50 | – | 1.35 | – | 24.15 | 1.53 | 18.57 | 3.16 | 44.48 | 3.09 | 2.17 |
| Ni 601-P1 (Fig. 15a) | 18.34 | 1.69 | 0.57 | – | 24.78 | – | 7.32 | – | 47.30 | – | – |
| Ni 601 (Fig. 15b) | 20.55 | 1.67 | 0.35 | – | 25.64 | 0.61 | 9.24 | – | 41.94 | – | – |
| Ni 601 before test | 1.26 | 1.29 | 0.40 | 0.26 | 23.03 | 0.67 | 12.08 | – | 61.01 | – | – |

To understand the trend in composition of scales, additional EDS analysis of the surface of alloys RA 333 and Ni 601 before the test was conducted and the results are included in Table 6.

Comparison of the surface composition for alloy RA 333 (Table 6) before and after test showed that Si, W and Cr content increased, while Ni, Co and Fe content decreased. Also mapping data of the scale on the alloy RA 333 clearly show

tungsten and silicon oxide in the layer. Based on the data above we can conclude that higher content of Cr, W and Si in scale improves its corrosion protective properties.

Comparing of EDS analysis of the alloy Ni 601 outer surface before and after experiments (Table 6) showed that Cr and Al content was increased while Ni and Fe content decreased. The scale mainly consisted of Cr oxide together with aluminum. It was noticed that addition of aluminum to nickel-based alloys [29] plays an important role in the formation of a dense, protective layer on the substrate surface, protecting it against further degradation induced by the atmosphere in high-temperature applications.

## Conclusions

Corrosive attack of intermediate compounds formed during combustion of aqueous UAN fuel was tested by metallographic investigation of seven segments of the fuel inlet tube made of 316 SS in which the hot ignition occurred. The heaviest corrosion (general and intergranular) was found in the initial segments of the tube, where the fuel entered the reactor and was ignited.

The corrosion performances of coupons of two stainless steels 316L, 310S and five nickel alloys 600, 601, 617, 800H and RA333, exposed in the reactor (10 MPa, 520 °C) for 100 h to gases formed during the combustion of aqueous UAN were studied. Alloys containing >23 wt% chromium were found to be resistant to the tested atmosphere. Alloy RA 333 was found to be the most resistant to oxidation under the tested conditions and the scale on its surface consisted of Cr/W/Si oxides. Satisfactory resistance was found for alloy 601 and stainless steel 310S: a thin Cr/Ni together with Al film was formed on the 601 Ni alloy surface and a thin chromium-rich scale on the 310S. Alloys 600 and 617 suffer from the internal oxidation, while alloy 800H was subjected to localized corrosion. 316L SS samples exhibited the highest corrosion in comparison with other tested materials, but the attack on coupons was significantly weaker than it was on the 316 SS fuel inlet tube.

Future work should focus on characterizing materials to construct the fuel inlet tube, where the fuel ignites. It is concluded herein that high Cr-containing metals are favorable as construction materials for parts that are in contact with aqueous UAN intermediate combustion products at ∼500 °C and at least up to 10 MPa.

## References

1. A. Grinberg Dana, G. E. Shter and G. S. Grader, *RSC Advances* **4**, 2014 (10051).
2. A. Grinberg Dana, G. E. Shter and G. S. Grader, *RSC Advances* **4**, 2014 (34836).
3. A. Grinberg Dana, G. Tvil, L. Winter, G. E. Shter and G. S. Grader, *Fuel* **159**, 2015 (500).

4. A. Grinberg Dana, B. Mosevitzky, G. Tvil, M. Epstein, G. E. Shter and G. S. Grader, *Energy and Fuels* **30**, 2016 (2474).
5. A. Grinberg Dana, G. E. Shter and G. S. Grader, *Energy Technology* **3**, 2015 (976).
6. A. Grinberg Dana, G. E. Shter and G. S. Grader, *Energy Technology* **4**, 2016 (7).
7. O. Hollander and G. E. Geiger, *Materials Performance* **41**, 2002 (50).
8. J. R. Cahoon, *Corrosion* **58**, 2002 (166).
9. H. Uhlig and H. Mazille, *Corrosion* **28**, 1972 (427).
10. I. Kap, M. Starostin, G. E. Shter and G. S. Grader, *Materials and Corrosion* **63**, 2012 (571).
11. O. Elishav, G. E. Shter and G. S. Grader, *Fuel* **181**, 2016 (765).
12. B. Mosevitzky, A. Grinberg Dana, G. E. Shter and G. S. Grader, *Combustion and Flame* **166**, 2016 (295).
13. N. Mu, K. Jung, N. M. Yanar, F. S. Pettit, G. R. Holcomb, B. H. Howard and G. H. Meier, *Oxidation of Metals* **79**, 2013 (461).
14. N. Hussain, K. A. Shahid, I. H. Khan and S. Rahman, *Oxidation of Metals* **41**, 1993 (251).
15. F. Liu, J. E. Tang, A. Asteman, J. E. Svensson, L. G. Johansson and M. Halvarsson, *Oxidation of Metals* **71**, 2009 (77).
16. H. Asteman, J. E. Svensson and L. G. Johansson, *Corrosion Science* **44**, 2002 (2635).
17. Y. Nishiyama, N. Otsuka and T. Kudo, *Corrosion Science* **48**, 2006 (2064).
18. P. Kritzer, N. Boukis and E. Dinjus, *Corrosion* **56**, 2000 (1093).
19. A. Grinberg Dana, M. Starostin, G. E. Shter and G. S. Grader, *Oxidation of Metals* **82**, 2014 (491).
20. T. M. Pollock and S. Tin, *Journal of Propulsion and Power* **22**, 2006 (361).
21. V. Firouzdor, K. Sridharan, G. Cao, M. Anderson and T. R. Allen, *Corrosion Science* **69**, 2013 (281).
22. Incoloy alloy 800 Special Metals Corporation, http://www.specialmetals.com
23. W. Ren and R. Swindeman, ASME 2010 Pressure Vessels and Piping Conference: **6**, Parts A and B Bellevue, Washington, USA, 821 (2010)
24. D. H. Xia and J. L. Luo, *Transactions of Tianjin University* **21**, 2015 (234).
25. Inconel alloy 600 Special Metals Corporation, http://www.specialmetals.com.
26. P. M. Scott. in *Ni 600, 9th International Symposium of Environmental Degradation of Materials in Nuclear Power Systems—Water Reactors*, eds. F. P. Ford, S. M. Bruemmer and G. S. Was, (The Minerals, Metals & Materials Society (TMS), Warrendale, 1999), p. 3.
27. D. Van Rooyen, *Corrosion* **31**, 1975 (327).
28. Inconel alloy 601 Special Metals Corporation, http://www.specialmetals.com.
29. R. Pillai, H. Ackermann and K. Lucka, *Corrosion Science* **69**, 2013 (181).
30. H. Ackermann, G. Teneva-Kosseva, H. Köhne, K. Lucka and S. Richter, *Materials and Corrosion* **59**, 2008 (380).
31. C. Strubbe, V. Serban, G. Marginean and W. Brandl, http://konsys-t.tanger.cz/files/proceedings/04/reports/1172.pdf.
32. Inconel alloy 617 Special Metals Corporation, http://www.specialmetals.com.
33. J. Chapovaloff, F. Rouillard, K. Wolski and M. Pijolat, *Corrosion Science* **69**, 2013 (31).
34. G. Stein-Brzozowska, D. M. Florez, J. Maier and G. Scheffknecht, *Fuel* **108**, 2013 (521).
35. N. Otsuka and H. Fujikawa, *Corrosion* **5**, 1991 (240).
36. M. Akbari-Garakani and M. Mehdizadeh, *Materials and Design* **32**, 2011 (2695).
37. Z. Zeng, K. Natesan, Z. Cai and D. L. Rink, *Fuel* **117**, 2014 (133).
38. R. A. Page, J. E. Hack and R. D. Brown, *Metallurgical Transactions A* **15A**, 1984 (11).
39. M.G. Fontana, Corrosion Engineering, (3-d Edition, **3-18**, 1986).
40. D. Mandrino, M. Godec, M. Torkar and M. Jenko, *Surface and Interface Analysis* **40**, 2008 (285).